Neuron
NeuroResource

Wireless Recording in the Peripheral Nervous System with Ultrasonic Neural Dust

Dongjin Seo,[1,4] Ryan M. Neely,[2,4] Konlin Shen,[1] Utkarsh Singhal,[1] Elad Alon,[1] Jan M. Rabaey,[1] Jose M. Carmena,[1,2,3,5,*] and Michel M. Maharbiz[1,3,5,*]
[1]Department of Electrical Engineering and Computer Sciences
[2]Helen Wills Neuroscience Institute
[3]UCB/UCSF Joint Graduate Program in Bioengineering
University of California, Berkeley, Berkeley, CA 94720, USA
[4]Co-first author
[5]Co-senior author
*Correspondence: jcarmena@berkeley.edu (J.M.C.), maharbiz@berkeley.edu (M.M.M.)
http://dx.doi.org/10.1016/j.neuron.2016.06.034

SUMMARY

The emerging field of bioelectronic medicine seeks methods for deciphering and modulating electrophysiological activity in the body to attain therapeutic effects at target organs. Current approaches to interfacing with peripheral nerves and muscles rely heavily on wires, creating problems for chronic use, while emerging wireless approaches lack the size scalability necessary to interrogate small-diameter nerves. Furthermore, conventional electrode-based technologies lack the capability to record from nerves with high spatial resolution or to record independently from many discrete sites within a nerve bundle. Here, we demonstrate neural dust, a wireless and scalable ultrasonic backscatter system for powering and communicating with implanted bioelectronics. We show that ultrasound is effective at delivering power to mm-scale devices in tissue; likewise, passive, battery-less communication using backscatter enables high-fidelity transmission of electromyogram (EMG) and electroneurogram (ENG) signals from anesthetized rats. These results highlight the potential for an ultrasound-based neural interface system for advancing future bioelectronics-based therapies.

INTRODUCTION

Recent technological advances (Boretius et al., 2010; Delivopoulos et al., 2012) and fundamental discoveries (Bhadra and Kilgore, 2005; Pavlov and Tracey, 2012; Rosas-Ballina et al., 2011) have renewed interest in implantable systems for interfacing with the peripheral nervous system. Early clinical successes with peripheral neurostimulation devices, such as those used to treat sleep apnea (Strollo et al., 2014) or control bladder function in paraplegics (Creasey et al., 2001) have led clinicians and researchers to propose new disease targets ranging from diabetes to rheumatoid arthritis (Famm et al., 2013). A recently proposed roadmap for the field of bioelectronic medicines highlights the need for new electrode-based recording technologies that can detect abnormalities in physiological signals and be used to update stimulation parameters in real time. Key features of such technologies include high-density, stable recordings of up to 100 channels in single nerves, wireless and implantable modules to enable characterization of functionally specific neural and electromyographic signals, and scalable device platforms that can interface with small nerves of 100 μm diameter or less (Birmingham et al., 2014) as well as specific muscle fibers. Current approaches to recording peripheral nerve activity fall short of this goal; for example, cuff electrodes provide stable chronic performance but are limited to recording compound activity from the entire nerve. Single-lead intrafascicular electrodes can record from multiple sites within a single fascicle but do not enable high-density recording from discrete sites in multiple fascicles (Lefurge et al., 1991). Similarly, surface EMG arrays allow for very-high-density recording (Lapatki et al., 2004; Martinez-Valdes et al., 2016) but do not capture fine details of deep or small muscles. Recently, wireless devices to enable untethered recording in rodents (Lee et al., 2013; Szuts et al., 2011) and nonhuman primates (Foster et al., 2014; Schwarz et al., 2014; Yin et al., 2014), as well as mm-scale integrated circuits for neurosensing applications have been developed (Biederman et al., 2015; Denison et al., 2007; Muller et al., 2015). However, most wireless systems use electromagnetic (EM) energy coupling and communication, which becomes extremely inefficient in systems smaller than ~5 mm due to the inefficiency of coupling radio waves at these scales within tissue (Rabaey et al., 2011; Seo et al., 2013; see also Size Scaling and Electromagnetics in the Supplemental Information). Further miniaturization of wireless electronics platforms that can effectively interface with small-diameter nerves will require new approaches.

In contrast to EM, ultrasound offers an attractive alternative for wirelessly powering and communicating with sub-mm implantable devices (Charthad et al., 2015; Larson and Towe, 2011; Meng and Sahin 2013; Ozeri and Shmilovitz, 2010; Seo et al., 2014). Ultrasound has two advantages. First, the speed of sound is 10^5 × lower than the speed of light in water, leading to much smaller wavelengths at similar frequencies; this yields excellent

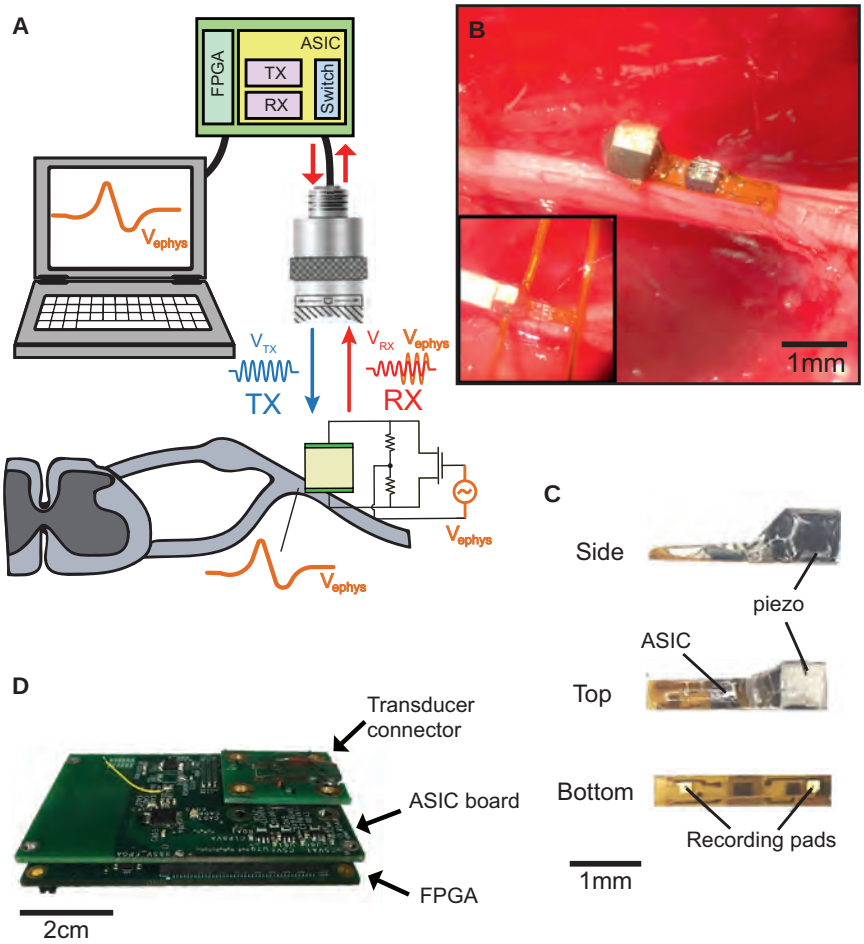

Figure 1. Neural Dust System Overview

(A) An external transducer powers and communicates with a neural dust mote placed remotely in the body. Driven by a custom transceiver board, the transducer alternates between transmitting a series of pulses that power the device and listening for reflected pulses that are modulated by electrophysiological signals.

(B) A neural dust mote anchored to the sciatic nerve in an anesthetized rat. Inset shows neural dust mote with optional testing leads.

(C) Components of a neural dust mote. The devices were assembled on a flexible PCB and consist of a piezoelectric crystal, a single custom transistor, and a pair of recording electrodes.

(D) The transceiver board consisted of Opal Kelly FPGA board, application-specific integrated circuit (ASIC) board (Seo et al., 2015; Tang et al., 2015), and the transducer connector board.

spatial resolution at these lower frequencies as compared to radio waves. Second, ultrasonic energy attenuates far less in tissue than EM radiation; this not only results in much higher penetration depths for a given power, but also significantly decreases the amount of unwanted power introduced into tissue due to scattering or absorption. In fact, for most frequencies and power levels, ultrasound is safe in the human body. These limits are well defined, and ultrasound technologies have long been used for diagnostic and therapeutic purposes. As a rough guide, about 72× more power is allowable into the human body when using ultrasound as compared to radio waves (Food and Drug Administration, 2008; International Committee on Electromagnetic Safety, 2006).

We previously introduced the *neural dust* ultrasonic backscattering concept to harness the potential advantages of ultrasound and showed that, theoretically, such a system could be scaled well below the mm-scale when used for wireless electrophysiological neural recording (Seo et al., 2013, 2014). Here, we present the first experimental validation of a neural dust system in vivo in the rat peripheral nervous system (PNS) and skeletal muscle, reporting both electroneurogram (ENG) recordings from the sciatic nerve and electromyographic (EMG) recordings from the gastrocnemius muscle. The neural dust system consists of an external ultrasonic transceiver board which powers and communicates with a millimeter-scale sensor implanted into either a nerve or muscle (Figure 1A). The implanted mote consists of a piezoelectric crystal, a single custom transistor, and a pair of recording electrodes (Figures 1B, 1C, and S1).

During operation, the external transducer alternates between (1) emitting a series of six 540-ns pulses every 100 μs and (2) listening for any reflected pulses. The entire sequence of transmit, receive, and reconstruction events are detailed in Figure 2; this sequence (steps A–H) is repeated every 100 μs during operation. Briefly, pulses of ultrasonic energy emitted by the external transducer impinge on the piezocrystal and are, in part, reflected back toward the external transducer. In addition, some of the ultrasonic energy causes the piezocrystal to vibrate; as this occurs, the piezocrystal converts the mechanical power of the ultrasound wave into electrical power, which is supplied to the transistor. Any extracellular voltage change across the two recording electrodes modulates the transistor's gate, changing the amount of current flowing between the terminals of the crystal. These changes in current, in turn, alter the vibration of the crystal and the intensity of the reflected ultrasonic energy. Thus, the shape of the reflected *ultrasonic* pulses encodes the *electrophysiological voltage* signal seen by the implanted electrodes and this electrophysiological signal can be reconstructed externally. The performance specifications of neural dust in comparison to other state-of-the-art systems are summarized in Table 1.

RESULTS

Commercially Available Components Can Be Assembled into mm-Scale Recording Implants

The assembly process (Figure S1A) shows a neural dust implant mote integrated on a 50-μm-thick polyimide flexible printed circuit board (PCB) where both the piezocrystal (0.75 × 0.75 ×

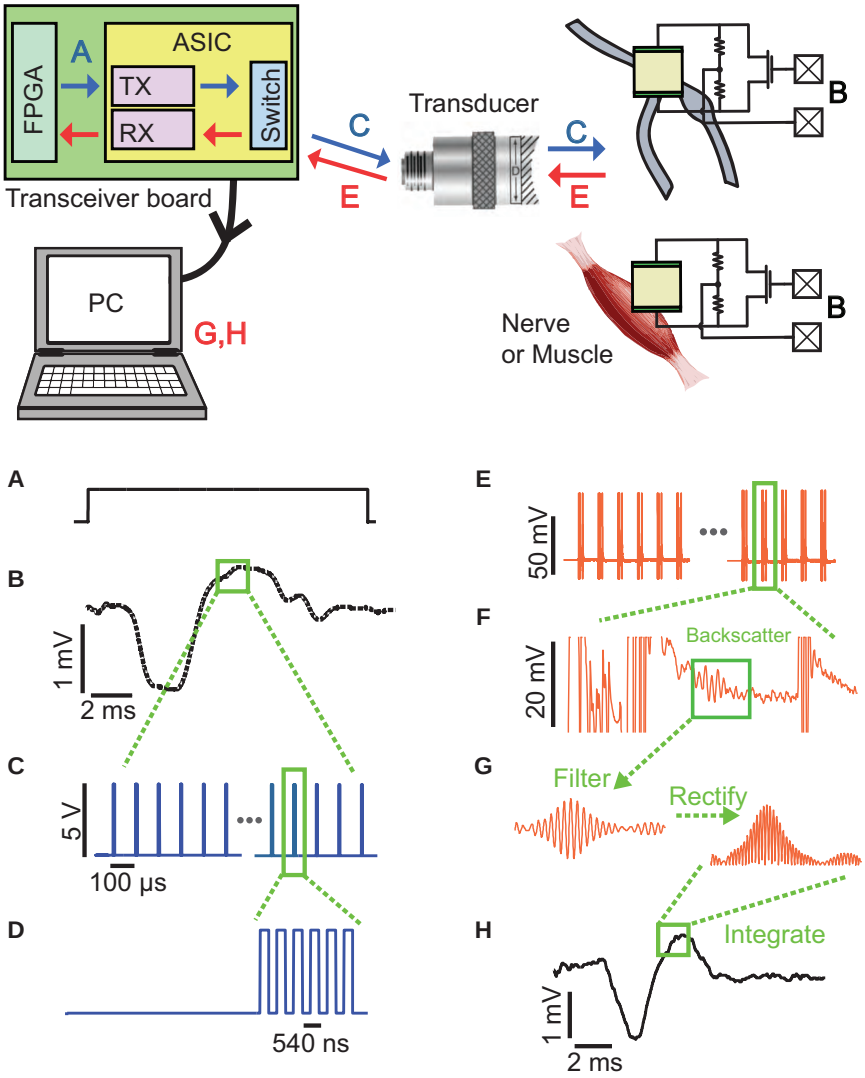

Figure 2. Neural Dust Measurement System and Wireless Backscatter

(Top) Schematic flow of information; (Bottom) representative time traces of signals at each step (referenced to the left diagram). The sequence is for reconstruction at one time point.

(A) The FPGA generates a trigger signal to initiate recording.

(B) An extracellular, electrophysiological potential is presented to the recording electrodes on a neural dust mote.

(C) Upon receiving the trigger from the FPGA, the transceiver board generates a series of transmit pulses. At the end of the transmit cycle, the switch on the ASIC disconnects the transmit module and connects the receive module.

(D) Zoomed-in transmit pulse sequence, showing 6 pulses at 1.85 MHz.

(E) Backscatter from the neural dust mote reaches the transducer approximately $2t_{Rayleigh}$.

(F) Zoomed-in backscatter waveforms, aligned in time with (E). Note the large, saturating signal which overlaps with the transmitted pulses is electrical feedthrough and is ignored. The returning, backscattered pulses can be seen subsequent to the transmission window (green box). A close up of the backscatter pulses is shown in Figure 3E and discussed in the text.

(G) These backscattered pulses are filtered and rectified, and the area under the curve is computed in order to produce reconstructed waveforms.

(H) Reconstructed waveform is sampled at 10 kHz. Each point of the reconstructed waveform is computed by calculating the area under the curve of the appropriate reflected pulses, received every 100 µs.

0.75 mm) and the custom transistor (0.5 × 0.45 mm) are attached to the topside of the board with a conductive silver paste. Electrical connections between the components are made using aluminum wirebonds and conductive gold traces. Exposed gold recording pads on the bottom of the board (0.2 × 0.2 mm) are separated by 1.8 mm and make contact on the nerve or muscle to record electrophysiological signals (Figure 1C). Recorded signals are sent to the transistor's input through micro-vias. Additionally, some implants were equipped with 0.35-mm-wide, 25-mm-long, flexible, compliant leads (Figure S1B) with test points for simultaneous measurement of both the voltage across the piezocrystal and direct wired measurement of the extracellular potential across the electrode pair used by the mote (we refer to this direct, wired recording of extracellular potential as the *ground truth measurement* below, which is used as a control for the ultrasonically reconstructed data). The entire implant is encapsulated in a medical grade UV-curable epoxy to protect wirebonds and provide insulation. A single neural dust mote implant measures roughly 0.8 × 3 × 1 mm (Figures 1C and S1). The size of the implants presented here is limited only by our use of commercial polyimide backplane technology, which is commercially accessible to anyone; relying on more aggressive assembly techniques with in-house polymer patterning would produce implants not much larger than the piezocrystal dimensions (yielding an ~1-mm^3 implant).

A Custom Integrated Circuit Operates the External Transceiver Board and Enables Low-Noise Interrogation

An external, ultrasonic transceiver board (Figure 1D) interfaces with neural dust motes by both supplying power (transmit [TX] mode) and receiving reflected signals (receive [RX] mode). This system is a low-power, programmable, and portable transceiver board that drives a commercially available external ultrasonic transducer (V323-SU, Olympus). Details of the custom integrated circuit (IC) that drove the external ultrasonic transducer with high-energy efficiency were presented elsewhere (Seo et al., 2015; Tang et al., 2015). The transceiver board exhibited a de-rated focus at ~8.9 mm (Figure 3A). The XY cross-sectional beam pattern clearly demonstrated the transition from the near-field to far-field propagation of the beam, with the narrowest beam at the Rayleigh distance (Figure 3B). The transducer was

Table 1. Performance Specifications of Neural Dust in Comparison to Other State-of-the-Art Systems

	Biederman et al., 2013	Muller et al., 2015	Schwerdt et al., 2011	Kiourti et al., 2016	Charthad et al., 2015	This Work (Neural Dust)
Power source	wireless (RF)	wireless (RF)	wireless (RF)	wireless (RF)	wireless (US)	wireless (US)
Gain (dB)	46	30	–	–	–	N/A
Bandwidth (kHz)	10	0.5	3	5	–	>30
TX frequency	1.5 GHz	300 MHz	2.2–2.45 GHz	2.4 GHz	1 MHz	1.85 MHz
Resolution (bits)	10	15	–	–	–	8 (digitizer)
Noise floor (μV_{rms})	6.5	1.2	500	63 (in vitro)	–	180
No. of channels	4	64	1	1	1	1
Total TX power (mW)	50	12	47	40	0.36	0.12
Avg. power (per ch) (μW)	2.63	3.52	0	0	85	0
Wireless data rate (Mbps)	1	1	–	–	–	0.5
Range in tissue (mm)	0.6	10	15	13	30	8.8
Volume (per ch) (mm^3)	– (ASIC)	– (ASIC)	24	360	45	2.4

Note that the noise floor measured for this work was carried out in a water tank. Avg., average; ch, channel.

driven with a 5-V peak-to-peak voltage signal at 1.85 MHz. The measured de-rated peak rarefaction pressure was 14 kPa, resulting in a mechanical index (MI) of 0.01. De-rated spatial pulse peak average (I_{SPPA}) and spatial peak time average (I_{SPTA}) of 6.37 mW/cm^2 and 0.21 mW/cm^2 at 10-kHz pulse repetition were 0.0034% and 0.03% of the FDA regulatory limit, respectively (Food and Drug Administration, 2008). The transceiver board was capable of outputting up to 32 V peak to peak, and the output pressure increased linearly with the input voltage (Figure 3C).

Reflections from Non-piezocrystal Interfaces Provide a Built-in Reference for Movement Artifacts and Temperature Drift

The entire system was submerged and characterized in a custom-built water tank with manual 6-degrees of freedom (DOF) linear translational and rotational stages (Thorlabs). Distilled water was used as a propagation medium, which exhibits similar acoustic impedance as tissue, at 1.5 MRayls (Kino, 1987). For initial calibration of the system, a current source (2400-LV, Keithley) was used to mimic extracellular signals by forcing electrical current at varying current densities through 0.127-mm-thick platinum wires (773000, A-M Systems) immersed in the tank. The neural dust mote was submerged in the current path between the electrodes. As current was applied between the wires, a potential difference arose across the implant electrodes. This potential difference was used to mimic extracellular electrophysiological signals during tank testing.

To interrogate the neural dust mote, six 540-ns pulses every 100 μs were emitted by the external transducer (Figure 2). These emitted pulses reflect off the neural dust mote and produce backscatter pulses back toward the external transducer. Reflected backscatter pulses were recorded by the same transceiver board (Figures 1A and 1D). The received backscatter waveform exhibits four regions of interest; these are pulses reflecting from four distinct interfaces (Figures 3D and 3E): (1) the water-polymer encapsulation boundary, (2) the top surface of the piezoelectric crystal, (3) the piezo-PCB boundary, and (4) the back of the PCB. As expected, the backscatter amplitude of the signals reflected from the piezoelectric crystal (second region) changed as a function of changes in potential at the recording electrodes. Reflected pulses from other interfaces did not respond to changes in potential at the recording electrodes. Importantly, pulses from the other non-responsive regions were used as a signal level reference, making the system robust to motion or heat-induced artifacts (snce pulses reflected from all interfaces change with physical or thermal disturbances of the neural dust mote but only pulses from the second region change as a function of electrophysiological signals). In a water tank, the system showed a linear response to changes in recording electrode potential and a noise floor of ~0.18 mV$_{rms}$ (Figure 3F). The overall dynamic range of the system is limited by the input range of the transistor and is greater than >500 mV (i.e., there is only an incremental change in the current once the transistor is fully on [input exceeds its threshold voltage] or fully off). The noise floor increased with the measured power drop-off of the beam; 0.7 mm of misalignment degraded it by a factor of two (n = 5 devices, Figure 3H). This lateral misalignment-induced increase in the noise floor constitutes the most significant challenge to neural recordings without a beam-steering system (that is, without the use of an external transducer array that can keep the ultrasonic beam focused on the implanted dust mote and, thus, on axis). On axis, the neural dust mote converted incident acoustic power to electrical power across the load resistance of the piezo with ~25% efficiency. Figure 3G plots the off-axis drop-off of voltage and power at one Rayleigh distance for the transducer used in this manuscript. Likewise, Figure 3I plots the change in effective noise floor as a function of angular misalignment.

EMG and ENG Can Be Recorded Tetherlessly In Vivo in Rodents

We recorded evoked EMG responses from the gastrocnemius muscle of adult Long-Evans rats under anesthesia using the neural dust system. The mote was placed on the exposed muscle surface, the skin and surrounding connective tissue were then

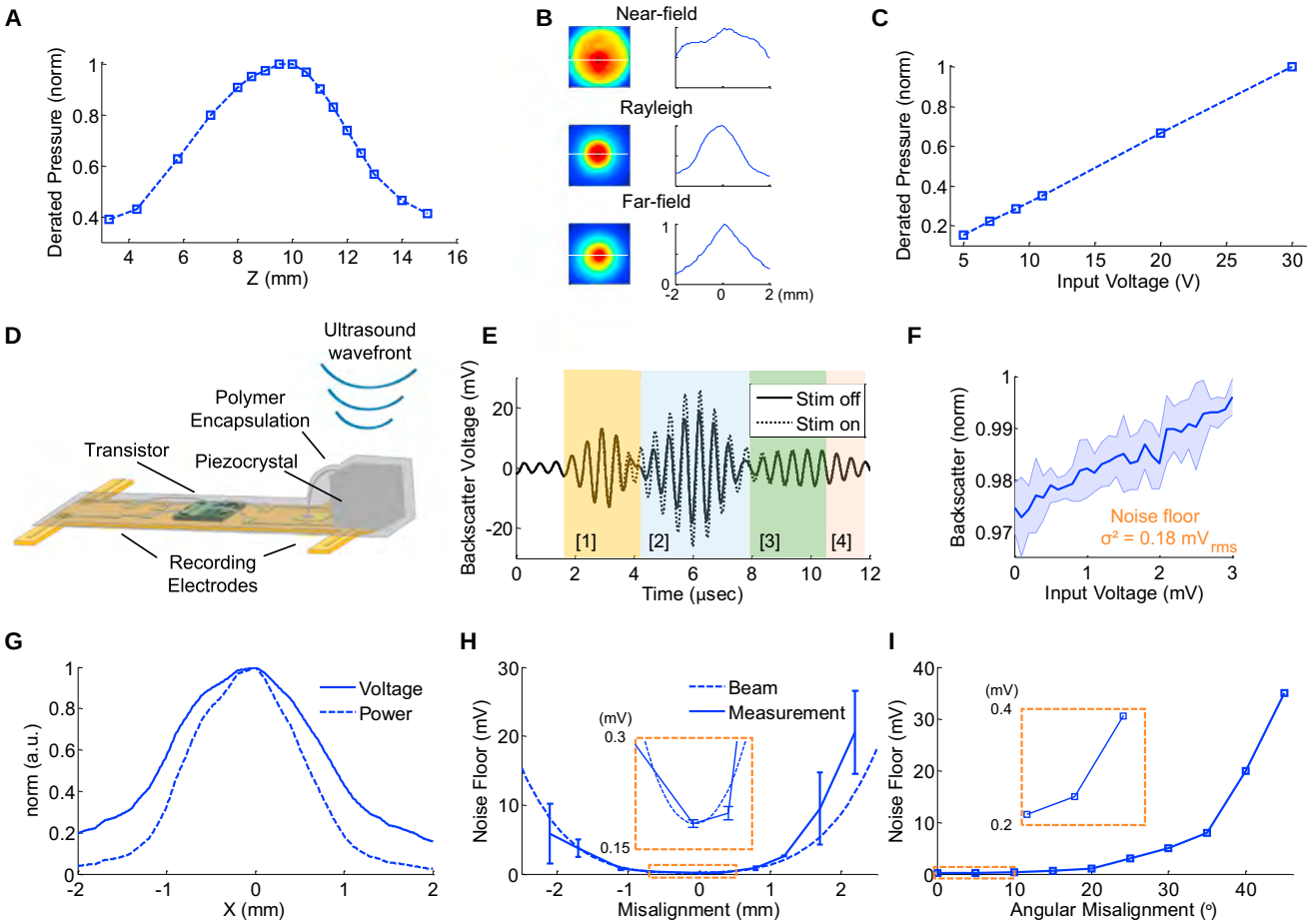

Figure 3. Power and Backscatter

(A) A de-rated, normalized peak pressure as a function of distance from the surface of the transducer showed a de-rated focus at ~8.9 mm at 1.85 MHz.

(B) The XY cross-sectional beam patterns and the corresponding 1D voltage plot at y = 0 at near-field, Rayleigh distance, and far-field showed beam focusing at the Rayleigh distance.

(C) The transducer's output pressure was a linear function of input voltage (up to 32 V peak to peak).

(D) Cross-section of the neural dust mote.

(E) Example backscatter waveform showing different regions of backscatter. The backscatter waveform is found flanked (in time) by regions which correspond to reflections arising from non-responsive regions; these correspond to reflected pulses from other device components shown in (D). The measurement from the non-responsive regions, which do not encode biological data, can be used as a reference. As a result of taking this differential measurement, any movements of the entire structure relative to the external transducer during the experiment can be subtracted out.

(F) Calibration curve obtained in the custom water tank setup showed the noise floor of 0.18 mV_{rms}.

(G) 1D plot of the transducer's off-axis voltage and power drop-off at y = 0 at Rayleigh distance.

(H) The effect of noise floor as a function of lateral misalignment followed the beam pattern power fall-off.

(I) Plot of drop in the effective noise floor as a function of angular misalignment. Angular misalignment results in a skewed beam pattern: ellipsoidal as opposed to circular. This increases the radius of focal spot (spreading energy out over a larger area); the distortion of the focal spot relaxes the constraint on misalignment.

replaced, and the wound was closed with surgical suture (Figure 4A). The ultrasonic transducer was positioned 8.9 mm away from the implant (one Rayleigh distance of the external transducer) and commercial ultrasound gel (Aquasonic 100, Parker Labs) was used to enhance coupling. The system was aligned using a manual manipulator by maximizing the harvested voltage on the piezocrystal measured from the flexible leads. Ag/AgCl wire hook electrodes were placed approximately 2 cm distally on the trunk of the sciatic nerve for the bulk stimulation of muscle fiber responses. Stimulation pulses of 200 μs duration were applied every 6 s, and data were recorded for 20 ms around the stimulation window (Figure 4B). The power spectral density (PSD) of the reconstructed data with several harmonics due to edges in the waveform is shown in Figure 4C. This process could be continued indefinitely, within the limit of the anesthesia protocol; a comparison of data taken after 30 min of continuous recording showed no appreciable degradation in recording quality (Figure 4D).

We obtained EMG recruitment curves with both ground truth and wireless dust backscatter by varying stimulation amplitude (Figures 5A and 5B). Reconstruction of the EMG signal from the wireless backscatter data was sampled at 10 kHz, while

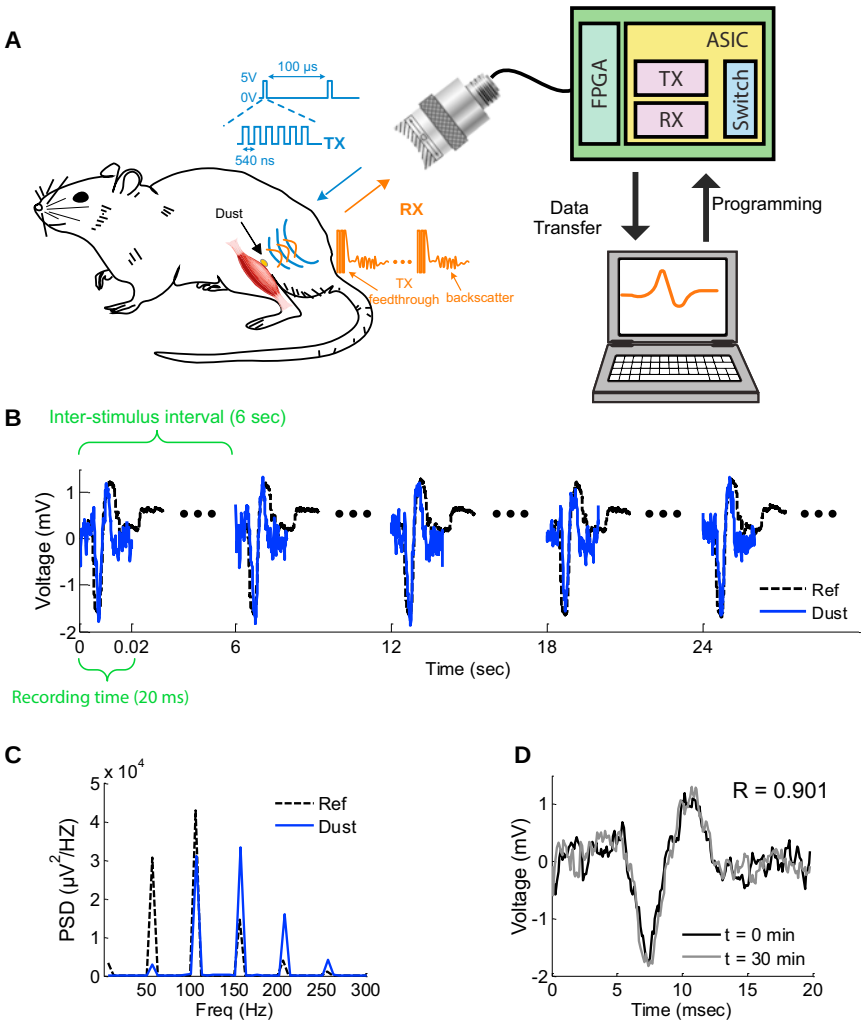

Figure 4. Tether-less Neural Dust Rodent EMG

(A) In vivo experimental setup for EMG recording from gastrocnemius muscle in rats; the neural dust mote was placed on the exposed muscle surface, and the wound was closed with surgical suture. The external transducer couples ultrasound to the mote, and the wireless data are recorded and displayed on the laptop.

(B) Comparison between ground truth measurement and the reconstructed EMG signals over a number of trials. 20-m samples were recorded, and the inter-stimulus interval was 6 s.

(C) Power spectral density (PSD) of the recorded EMG signal showed 4.29e4 μV^2/Hz and 3.11e4 μV^2/Hz at 107 Hz for ground truth and the reconstructed dust data, respectively, and several harmonics due to edges in the waveform.

(D) The wireless backscatter data recorded at t = 0 min and t = 30 min matched with R = 0.901.

the wired, ground truth measurement was sampled at 100 kHz with a noise floor of 0.02 mV. The two signals at response-saturating stimulation amplitude (100%) matched with R = 0.795 (Figure 5C). The difference between the wireless and wired data was within ± 0.4 mV (Figure 5D). The salient feature of the neural dust mote EMG response was approximately 1 ms narrower than the ground truth, which caused the largest error in the difference plot (Figures 5C and 5D). The responses from skeletal muscle fibers occurred 5 ms post-stimulation and persisted for 5 ms. The peak-to-peak voltage of the EMG shows a sigmoidal response as a function of stimulation intensity (Figure 5E) as expected (Gruner and Mason, 1989). The error bars indicate the measurement uncertainties from two rats and ten samples each per stimulation amplitude. The minimum signal detected by the neural dust mote is approximately 0.25 mV, which is in good agreement with the noise floor measurement made in a water tank.

A similar setup was prepared to measure the electroneurogram (ENG) response from the main branch of the sciatic nerve in anesthetized rats. The sciatic nerve was exposed by separating the hamstring muscles and the neural dust mote was placed and sutured to the nerve, with the recording electrodes making contact with the epineurium (Figure 1B). We measured a similar graded response on both ground truth and wireless dust backscatter by varying stimulation current amplitude delivered to bipolar stainless steel electrodes placed in the foot (Figures 6A and 6B). The two signals at response-saturating stimulation amplitude (100%) matched with R = 0.886 (Figure 6C); the average error was within ±0.2 mV (Figure 6D). The peak-to-peak ENG voltage showed a sigmoidal response with the error bars indicating uncertainties from two rats and ten samples each per stimulation amplitude. The minimum signal detected by the neural dust mote was again at 0.25 mV (Figure 6E).

DISCUSSION

In recent years, there has been growing interest in the use of neural recording technologies to improve neurostimulation-based treatments as well as to develop new closed-loop neuromodulation therapies for disorders in the central (Krook-Magnuson et al., 2015) and peripheral (Famm et al., 2013) nervous systems. Because nerves carry both efferent and afferent signals to a variety of target organs, effective recording technologies will need high spatiotemporal resolution to record from multiple discrete sites within a single nerve. In order for these technologies to become clinically viable they will need to be tether-less to avoid potential infections and adverse biological responses due to micro-motion of the implant within the tissue.

To address this looming issue, we designed, built, and implanted a wireless, ultrasonic neural sensor and communication system that enables neural recordings in the peripheral nervous system. In vivo, acute recordings in a stationary, anesthetized rat

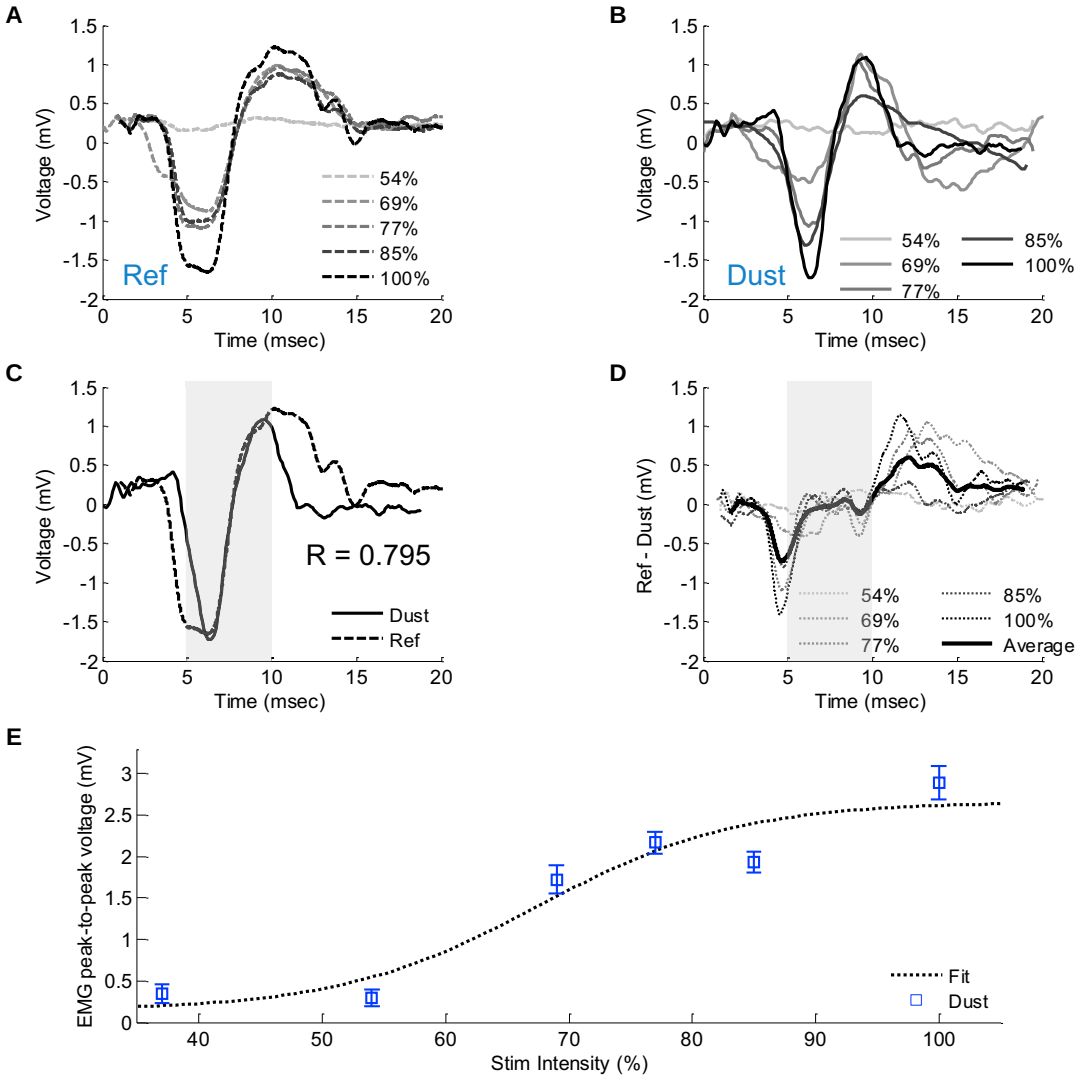

Figure 5. Tether-less Neural Dust Rodent Graded EMG

(A) Different intensities of EMG signals were recorded in vivo with the electrodes on the PCB with varying stimulation intensities.

(B) Similar gradient EMG responses were recorded wirelessly with the mote.

(C) Ground truth and reconstruction of EMG signal from the wireless backscatter data at response-saturating stimulation amplitude (100%) matched with R = 0.795 (R = 0.60, 0.64, 0.67, 0.92 for 54%, 69%, 77%, 89%, respectively).

(D) Quantitative comparison showed <0.4 mV match of the salient feature (shaded regions).

(E) EMG peak-to-peak voltage showed an expected sigmoidal relationship with the stimulation intensity.

model were used to collect compound action potentials from the main branch of the sciatic nerve as well as evoked EMG from the gastrocnemius muscle. The performance of the neural dust system was equivalent to conventional electrophysiological recordings employing microelectrodes and cabled electronics.

One of the principal strengths of the demonstrated technology is that, unlike conventional radio frequency technology, ultrasound-based systems appear scalable down to <100 μm sizes (see Size Scaling and Electromagnetics in the Supplemental Information), opening the door to a new technological path in implantable electronics. A complete analysis of this scaling can be found in (Seo et al., 2013, 2014). In brief, physics limits how small a good radio frequency receiver can be due to the long wavelengths of radio frequency energy (millimeters to centimeters) and the high degree of absorption of radio frequency energy into tissue (which heats up the tissue and limits the total power than can be sent to an implant). Ultrasonic systems fare much better in both areas, allowing for the design of extremely small receiver devices. In addition, the extreme miniaturization of lower power electronics allows for useful recording electronics to be incorporated into such small packages.

A number of technical challenges remain open. The power levels used in this study were limited by the specifications of commercially available transducers; custom transducers will

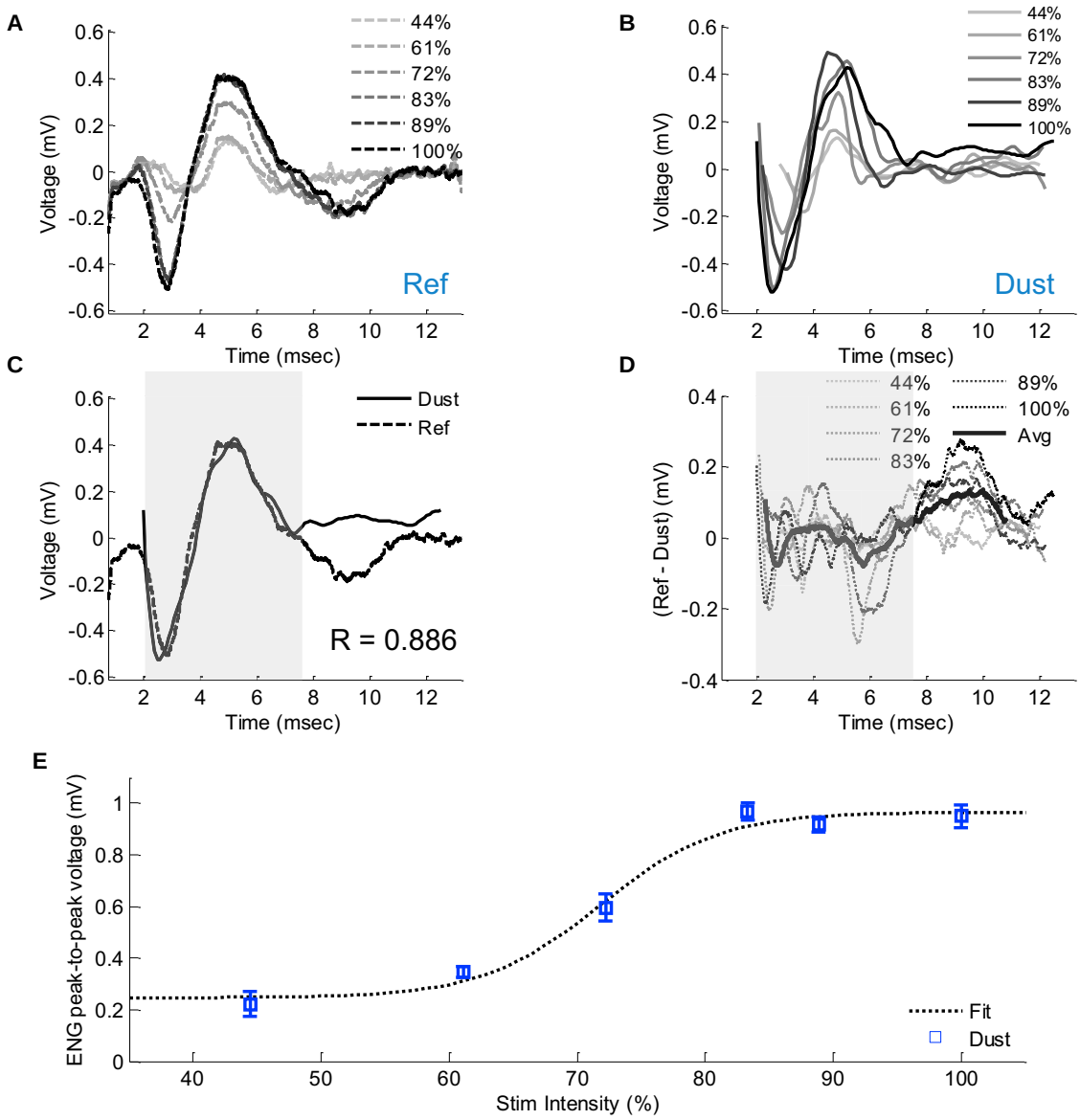

Figure 6. Tether-less Neural Dust Rodent Graded ENG

(A) Different intensities of ENG signals were recorded in vivo with the electrodes on the PCB with varying stimulation intensities.

(B) Similar gradient ENG responses were recorded wirelessly with the mote.

(C) Ground truth and reconstruction of ENG signal from the wireless backscatter data at response-saturating stimulation amplitude (100%) matched with R = 0.886 (R = 0.822, 0.821, 0.69, 0.918, 0.87 for 44%, 61%, 72%, 83%, 89%, respectively).

(D) Quantitative comparison showed <0.2 mV match of the salient feature (shaded regions).

(E) ENG peak-to-peak voltage showed an expected sigmoidal relationship with the stimulation intensity.

reduce the overall external device footprint, lower the noise floor (by producing higher power densities at the focal spot), and allow for selection of the focal depth to suit specific applications. For example, a flat, low-profile piezo transducer with proper impedance matching would enable a wearable neural dust transceiver board small enough for awake, behaving rodent neurophysiology. Additionally, the development of wearable, battery-powered multi-element arrays would allow for beam steering of the ultrasonic beam, with several advantages: (1) motes could be maintained on axis even in the face of relative motion between mote and external transducer, which is the most significant challenge of the present work; (2) multiple motes could potentially be interrogated by sweeping the focused beam electronically; (3) post-surgical tuning of mote location would be made easier. Additional de-noising of the transceiver drive electronics should also help decrease the noise floor (see Experimental Procedures). The modifications above are all well-within current state of the art; with others, we have recently shown theoretical and

experimental advantages to using beam-forming systems (Bertrand et al., 2014; Seo et al., 2015).

In addition, the calculated scaling predictions suggest that <500-μm scale motes are feasible. To do this, a number of material and microfabrication challenges exist, including the use of microfabricated backplanes, solder microbumping assembly of components (instead of the conventional wirebonding approach used here), and the use of thin film encapsulants (instead of medical grade epoxy) such as parylene. Transitioning away from PZT piezocrystals to biocompatible $BaTiO_3$ single crystal transducers is also under way; taken together, these developments would open the way for chronic studies of neural dust recording.

Last, as this platform presents a generalized power delivery system, the design and fabrication of neural stimulation systems based on charge delivery through electrodes on the dust motes is also under way.

EXPERIMENTAL PROCEDURES

Neural Dust Mote Assembly

Lead zirconate titanate (PZT) sheets (841, APC International) with ~12 μm of fired on silver were diced to desired dimensions using a dicing saw (DAD3240, Disco) with a ceramic blade (PN CX-010-270-080-H). The diced PZT coupon, along with the custom transistor, was attached to a 50-μm-thick polyimide flexible PCB with immersion gold (Altaflex) using a thin layer of two-part silver epoxy with 1:1 mix ratio (H20E, Epotek). The board was cured at 150°C, which is far below the melting temperature of polyimide and the Curie temperature of the PZT, for 10 min. The custom transistor was wirebonded using an aluminum ultrasonic wirebonder (7400B, West Bond) to pre-patterned targets. In order to prevent charge build-up on the PZT from the wedge contact, top and bottom contacts of the PZT were discharged to a thin metal sheet prior to wirebonding the top contact of the PZT to close the circuits. Medical-grade, UV-curable epoxy (OG116-31, Epotek) was used to protect the wirebond and provide insulation. The platform was then cured in UV chamber (Flash, Asiga) with 92 mW/cm^2 at 365 nm for 3 min.

Electrical and Ultrasonic Characterization of the Assembly in Water

The custom transistor was electrically tested with a precision current meter (2400-LV, Keithley) and a DC power supply (3631A, Agilent). To characterize the piezocrystal prior to assembly, an impedance plot was obtained with an impedance analyzer (4285A, Agilent) using two-terminal measurements with open/short/load calibration scheme. The impedance of exposed gold recording pads (0.2 × 0.2 mm), separated by 1.8 mm on the bottom of the PCB, was measured in Phosphate Buffered Solution (PBS 1×) with an electrochemical impedance spectroscope (nanoZ, White Matter). The device formed the active electrode and a silver wire formed the reference electrode.

Ultrasonic characterization of the transducer was performed in a custom-built water tank. A capsule hydrophone (HGL-0400, Onda) with 20 dB preamplification (AH-2020, Onda) was mounted on a computer-controlled 2D translating stage (XSlide, VelMex) and was used to calibrate the output pressure and characterize beam patterns of a 2.25 MHz single-element transducer (V323-SU, Olympus). Verification of ultrasonic power transfer and communication sensitivity was performed in a smaller water tank with the transducer mounted on manual translational and rotational stages (Thorlabs). The outline of the neural dust mote was patterned on an extruded acrylic piece with UV laser, and the mote was clamped to the acrylic stage with nylon screws. The position and angle of the transducer with relative to the mote were manually adjusted until the maximum voltage was measured across the piezocrystal. Cable capacitances and parasitics were carefully calibrated by adjusting the series capacitance in the high-impedance probes (N2863B, Agilent). An electric field in the water tank was generated with a current source (2400-LV, Keithley) forcing electrical current at varying current densities through two 0.127-mm-thick platinum wires (773000, A-M systems) immersed in the tank.

The transceiver board consisted of a custom integrated circuit (IC) in a QFN-64 package that achieved an on-chip 1.8- to 32-V charge pump efficiency of 33% and system latency of 20 ns and consumed 16.5 μJ per each transmit cycle (Tang et al., 2015). During the receive mode, the high-voltage switch was closed, and the signal was amplified by 28 dB; both operations were performed on chip. The output signal from the chip was digitized by an off-chip 10-bit, 100 MHz analog-to-digital converter (ADC) (LTC2261-12, Linear Technology). The outputs of the ADC were fed back into the field-programmable gate array (FPGA) and USB 3.0 integration module (XEM6310-LX45, Opal Kelly) and transferred to the laptop. The FPGA-USB module was also used to serially program the IC.

Experiment Setup and Surgical Procedures

All animal procedures were performed in accordance with University of California Berkeley Animal Care and Use Committee regulations. Adult male Long-Evans rats were used for all experiments. Prior to the start of surgery, animals were anesthetized with a mixture of ketamine (50 mg/kg) and xylazine (5 mg/kg) intraperitoneally (i.p.). The fur surrounding the surgical site was shaved and cleaned. For EMG recordings, a patch of gastrocnemius muscle roughly 10 × 5 mm in size was exposed by removing the overlying skin and fascia. The neural dust mote was then placed on the exposed muscle, the skin and fascia were replaced, and the wound was closed with 5/0 surgical suture. For ENG recordings, the sciatic nerve was exposed by making an incision from the sciatic notch to the knee, and separating the hamstring muscles. The mote was then placed in contact with the epineurium of the main branch of the sciatic nerve bundle and sutured to the nerve using 10/0 microsurgical suture. Animals were euthanized at the conclusion of the experiments.

Constant-current stimulation was delivered using an isolated pulse stimulator (2100, A-M Systems). Single biphasic pulses with a 2-ms pulse width were used to deliver stimulation at various current amplitudes. For each experiment, electrophysiological responses from ten stimulations (i.e., samples) were recorded. The FPGA-USB module generated a trigger for the stimulator every 6 s. For EMG experiments, bipolar Ag-AgCl hook electrodes placed around the trunk of the sciatic nerve were used for stimulation. To evoke ENG activity, 28G stainless steel needle electrodes were placed in the foot with an inter-electrode distance of approximately 5 mm.

The wired signals were amplified (100×) by a battery-powered differential amplifier with a built-in band-pass filter (DAM50, WPI) set at 10 Hz to 1 kHz. The ground reference for the amplifier was a 28G stainless steel needle electrode placed in the contralateral foot relative to the recording setup. The output of the amplifier was connected to a multi-channel digitizer, sampled at 100 kHz, and recorded on computer.

Transmit Pulse Waveforms and Data Acquisition

The neural dust mote was placed one Rayleigh distance from the transducer (8.9 mm), which corresponded to 5.9 μs transit time, assuming an acoustic velocity of ~1,500 m/s in water. Six cycles of square waves at 1.85 MHz with peak voltage of 5 V were launched every 100 μs (pulse repetition frequency [PRF] of 10 kHz). The total transmit pulse width was approximately, 3.3 μs, which was sufficiently small to prevent any overlaps with the first harvested voltage measurement at 5.9 μs. Given that the first reflection back to the transducer (e.g., backscatter) occurred at approximately 11.8 μs (twice the transit time) and persisted until for 3.3 μs, the maximum PRF (e.g., in this context, the sampling rate) was ~66 kHz. Given that the bulk peripheral nerve responses occurred below 1 kHz (Mezzarane et al., 2013), a PRF of 10 kHz was chosen to sufficiently capture the dynamics.

In order to sample the backscatter waveform at 1.85 MHz without losing signal fidelity, the off-chip ADC on the transceiver board was heavily oversampled at 50 MHz. This resulted in ~8 Mbits of data in a 10-ms neural recording, which was stored in a 128 MByte, 16-bit wide, synchronous DDR2 DRAM (MT47H64M16HR-3, Micron Technology). The raw waveforms were transferred to the laptop via the USB interface post-recording. The raw waveforms were simultaneously recorded using an 8-bit digitizer (USB-5133, National Instruments) for comparison.

Backscatter Data Processing

Raw backscatter waveforms, sampled at 50 MHz, from each experiment were sliced and time aligned to be averaged over eight samples. The averaged

signals were band-pass filtered with a symmetric fourth order Butterworth filter from 10 Hz to 1 kHz. The distinct characteristics of the backscatter waveform (Figure 3E) were used as a template to locate the region of interest. The signals were then rectified, and the integral of the region was computed to estimate the input voltage signal, which exhibited a linear response (Figure 3F). Multiplication factor for the signal was extracted from the ground truth measurement.

SUPPLEMENTAL INFORMATION

Supplemental Information includes Supplemental Experimental Procedures and seven figures and can be found with this article online at http://dx.doi.org/10.1016/j.neuron.2016.06.034.

AUTHOR CONTRIBUTIONS

M.M.M., J.M.C., J.M.R., and E.A. conceived the idea for neural dust. D.S., E.A., and M.M.M. designed and taped out the backscatter chip. K.S., D.S., and M.M.M. designed and built the flexible PCB and the neural dust implants. D.S. designed and assembled the ultrasonic transceiver module, and D.S. and U.S. programmed the FPGA for data acquisition. R.M.N. and J.M.C. designed animal-testing experiments. R.M.N. and D.S. performed the experiments. D.S., R.M.N., and U.S. analyzed data. D.S., R.M.N., J.M.C., and M.M.M wrote the manuscript with contributions from all authors. M.M.M. and J.M.C. supervised the project.

ACKNOWLEDGMENTS

We thank H. Tang, N. Narevsky, R. Muller, M. Chamanzar, and M. Shapiro for fruitful discussion and advice; S. Parthasarathy, A. Ozilgen, and R. Sandrone for measurement assistance; Taiwan Semiconductor Manufacturing Company (TSMC) for chip fabrication; and Berkeley Wireless Research Center (BWRC), the Berkeley Sensor and Actuator Center (BSAC), and Marvell Nanofabrication staffs for technical assistance with assembly and fabrication. Funding was provided by the National Science Foundation Graduate Research Fellowship (D.S. and K.S.), the National Defense Science and Engineering Graduate Fellowship (R.M.N.), and the Defense Advanced Research Projects Agency (DARPA) BTO under the auspices of Dr. Doug Weber (HR0011-15-2-0006).

Received: January 7, 2016
Revised: March 30, 2016
Accepted: June 21, 2016
Published: August 3, 2016

REFERENCES

Bertrand, A., Seo, D., Maksimovic, F., Carmena, J.M., Maharbiz, M.M., Alon, E., and Rabaey, J.M. (2014). Beamforming approaches for untethered, ultrasonic neural dust motes for cortical recording: a simulation study. Proc. IEEE Eng. Med. Biol. Soc. *2014*, 2625–2628.

Bhadra, N., and Kilgore, K.L. (2005). High-frequency electrical conduction block of mammalian peripheral motor nerve. Muscle Nerve *32*, 782–790.

Biederman, W., Yeager, D.J., Narevsky, N., Koralek, A.C., Carmena, J.M., Alon, E., and Rabaey, J.M. (2013). A fully-integrated, miniature (0.125 mm^2) 10.5 μW wireless neural sensor. IEEE J. Solid State Circuits *48*, 960–970.

Biederman, W., Yeager, D.J., Narevsky, N., Leverett, L., Neely, R., Carmena, J.M., Alon, E., and Rabaey, J.M. (2015). A 4.78 mm2 fully-integrated neuromodulation SoC combining 64 acquisition channels with digital compression and simultaneous dual stimulation. IEEE J. Solid State Circuits *50*, 1038–1047.

Birmingham, K., Gradinaru, V., Anikeeva, P., Grill, W.M., Pikov, V., McLaughlin, B., Pasricha, P., Weber, D., Ludwig, K., and Famm, K. (2014). Bioelectronic medicines: a research roadmap. Nat. Rev. Drug Discov. *13*, 399–400.

Boretius, T., Badia, J., Pascual-Font, A., Schuettler, M., Navarro, X., Yoshida, K., and Stieglitz, T. (2010). A transverse intrafascicular multichannel electrode (TIME) to interface with the peripheral nerve. Biosens. Bioelectron. *26*, 62–69.

Charthad, J., Weber, M.J., Chang, T.C., and Arbabian, A. (2015). A mm-sized implantal medical device (IMD) with ultrasonic power transfer and a hybrid bidirectional data link. IEEE J. Solid State Circuits *50*, 1741–1753.

Creasey, G.H., Grill, J.H., Korsten, M., U, H.S., Betz, R., Anderson, R., and Walter, J.; Implanted Neuroprosthesis Research Group (2001). An implantable neuroprosthesis for restoring bladder and bowel control to patients with spinal cord injuries: a multicenter trial. Arch. Phys. Med. Rehabil. *82*, 1512–1519.

Delivopoulos, E., Chew, D.J., Minev, I.R., Fawcett, J.W., and Lacour, S.P. (2012). Concurrent recordings of bladder afferents from multiple nerves using a microfabricated PDMS microchannel electrode array. Lab Chip *12*, 2540–2551.

Denison, T., Consoer, K., Santa, W., Avestruz, A.T., Cooley, J., and Kelly, A. (2007). A 2uW 100 nV/rtHz chopper-stabilized instrumentation amplifier for chronic measurement of neural field potentials. IEEE J. Solid State Circuits *42*, 2934–2945.

Famm, K., Litt, B., Tracey, K.J., Boyden, E.S., and Slaoui, M. (2013). Drug discovery: a jump-start for electroceuticals. Nature *496*, 159–161.

Food and Drug Administration (2008). Information for manufacturers seeking market clearance of diagnostic ultrasound systems and transducers. http://www.fda.gov/downloads/UCM070911.pdf

Foster, J.D., Nuyujukian, P., Freifeld, O., Gao, H., Walker, R., I Ryu, S., H Meng, T., Murmann, B., J Black, M., and Shenoy, K.V. (2014). A freely-moving monkey treadmill model. J. Neural Eng. *11*, 046020.

Gruner, J.A., and Mason, C.P. (1989). Nonlinear muscle recruitment during intramuscular and nerve stimulation. J. Rehabil. Res. Dev. *26*, 1–16.

International Committee on Electromagnetic Safety (2006). IEEE standards for safety levels with respect to human exposure to radio frequency electromagnetic fields, 3 khz to 300 ghz. http://emfguide.itu.int/pdfs/C95.1-2005.pdf

Kino, G.S. (1987). Acoustic Waves: Devices, Imaging, and Analog Signal Processing, *Chapter 1*, First Edition (Prentice-Hall).

Kiourti, A., Lee, C.W.L., Chae, J., and Volakis, J.L. (2016). A wireless fully passive neural recording device for unobtrusive neuropotential monitoring. IEEE Trans. Biomed. Eng. *63*, 131–137.

Krook-Magnuson, E., Gelinas, J.N., Soltesz, I., and Buzsáki, G. (2015). Neuroelectronics and biooptics: closed-loop technologies in neurological disorders. J. Am. Med. Assoc. Neurol. *72*, 823–829.

Lapatki, B.G., Van Dijk, J.P., Jonas, I.E., Zwarts, M.J., and Stegeman, D.F. (2004). A thin, flexible multielectrode grid for high-density surface EMG. J. Appl. Physiol. *96*, 327–336.

Larson, P.J., and Towe, B.C. (2011). Miniature ultrasonically powered wireless nerve cuff stimulator. Proc. IEEE Eng. Med. Biol. Soc. *2011*, 265–268.

Lee, S.B., Yin, M., Manns, J.R., and Ghovanloo, M. (2013). A wideband dual-antenna receiver for wireless recording from animals behaving in large arenas. IEEE Trans. Biomed. Eng. *60*, 1993–2004.

Lefurge, T., Goodall, E., Horch, K., Stensaas, L., and Schoenberg, A. (1991). Chronically implanted intrafascicular recording electrodes. Ann. Biomed. Eng. *19*, 197–207.

Martinez-Valdes, E., Laine, C.M., Falla, D., Mayer, F., and Farina, D. (2016). High-density surface electromyography provides reliable estimates of motor unit behaviour. Clin. Neurophysiol. *127*, 2534–2541.

Meng, H., and Sahin, M. (2013). An electroacoustic recording device for wireless sensing of neural signals. Proc. IEEE Eng. Med. Biol. Soc. 3086–3088.

Mezzarane, R.A., Elias, L.A., Magalhaes, F.H., Chaud, V.M., and Kohn, A.F. (2013). Experimental and simulated EMG responses in the study of the human spinal cord. In Electrodiagnosis in New Frontiers of Clinical Research, H. Turker, ed. (InTech), pp. 57–87.

Muller, R., Le, H.P., Li, W., Ledochowitsch, P., Gambini, S., Bjorninen, T., Koralek, A., Carmena, J.M., Maharbiz, M.M., Alon, E., et al. (2015). A minimally invasive 64-channel wireless uECoG implant. IEEE J. Solid State Circuits *50*, 344–359.

Ozeri, S., and Shmilovitz, D. (2010). Ultrasonic transcutaneous energy transfer for powering implanted devices. Ultrasonics *50*, 556–566.

Pavlov, V.A., and Tracey, K.J. (2012). The vagus nerve and the inflammatory reflex–linking immunity and metabolism. Nat. Rev. Endocrinol. *8*, 743–754.

Rabaey, J.M., Mark, M., Chen, D., Sutardja, C., Tang, C., Gowda, S., Wagner, M., and Werthimer, D. (2011). Powering and communicating with mm-size implants. IEEE DATE, 1–6.

Rosas-Ballina, M., Olofsson, P.S., Ochani, M., Valdés-Ferrer, S.I., Levine, Y.A., Reardon, C., Tusche, M.W., Pavlov, V.A., Andersson, U., Chavan, S., et al. (2011). Acetylcholine-synthesizing T cells relay neural signals in a vagus nerve circuit. Science *334*, 98–101.

Schwarz, D.A., Lebedev, M.A., Hanson, T.L., Dimitrov, D.F., Lehew, G., Meloy, J., Rajangam, S., Subramanian, V., Ifft, P.J., Li, Z., et al. (2014). Chronic, wireless recordings of large-scale brain activity in freely moving rhesus monkeys. Nat. Methods *11*, 670–676.

Schwerdt, H.N., Xu, W., Shekhar, S., Abbaspour-Tamijani, A., Towe, B.C., Miranda, F.A., and Chae, J. (2011). A fully passive wireless microsystem for recording of neuropotential using RF backscattering methods. IEEE JMEMS *20*, 1119–1130.

Seo, D., Carmena, J.M., Rabaey, J.M., Alon, E., and Maharbiz, M.M. (2013). Neural dust: an ultrasonic, low power solution for chronic brain-machine interface. Published online July 8, 2013. arXiv:1307:2196. http://arxiv.org/abs/1307.2196

Seo, D., Carmena, J.M., Rabaey, J.M., Maharbiz, M.M., and Alon, E. (2014). Model validation of untethered, ultrasonic neural dust motes for cortical recording. J. Neurosci. Methods *244*, 114–122.

Seo, D., Tang, H., Carmena, J.M., Rabaey, J.M., Alon, E., Boser, B.E., and Maharbiz, M.M. (2015). Ultrasonic beamforming system for interrogating multiple implantable sensors. Proc. IEEE Eng. Med. Biol. Soc. 2673–2676.

Strollo, P.J., Jr., Soose, R.J., Maurer, J.T., de Vries, N., Cornelius, J., Froymovich, O., Hanson, R.D., Padhya, T.A., Steward, D.L., Gillespie, M.B., et al.; STAR Trial Group (2014). Upper-airway stimulation for obstructive sleep apnea. N. Engl. J. Med. *370*, 139–149.

Szuts, T.A., Fadeyev, V., Kachiguine, S., Sher, A., Grivich, M.V., Agrochão, M., Hottowy, P., Dabrowski, W., Lubenov, E.V., Siapas, A.G., et al. (2011). A wireless multi-channel neural amplifier for freely moving animals. Nat. Neurosci. *14*, 263–269.

Tang, H.Y., Seo, D., Singhal, U., Li, X., Maharbiz, M.M., Alon, E., and Boser, B.E. (2015). Miniaturizing ultrasonic system for portable health care and fitness. IEEE Trans. Biomed. Circuits Syst. *9*, 767–776.

Yin, M., Borton, D.A., Komar, J., Agha, N., Lu, Y., Li, H., Laurens, J., Lang, Y., Li, Q., Bull, C., et al. (2014). Wireless neurosensor for full-spectrum electrophysiology recordings during free behavior. Neuron *84*, 1170–1182.